# Initial nucleation of metastable y-Ga<sub>2</sub>O<sub>3</sub> during sub-millisecond thermal anneals of amorphous Ga<sub>2</sub>O<sub>3</sub>

Cite as: Appl. Phys. Lett. **121**, 062102 (2022); https://doi.org/10.1063/5.0087093 Submitted: 01 February 2022 • Accepted: 17 July 2022 • Published Online: 08 August 2022

🧓 Katie R. Gann, 🗓 Celesta S. Chang, 🗓 Ming-Chiang Chang, et al.

# **COLLECTIONS**

Paper published as part of the special topic on Wide- and Ultrawide-Bandgap Electronic Semiconductor Devices







ARTICLES YOU MAY BE INTERESTED IN

Degradation mechanisms of Mg-doped GaN/AIN superlattices HEMTs under electrical stress Applied Physics Letters 121, 062101 (2022); https://doi.org/10.1063/5.0094957

Generalized model of laser-induced peak asymmetry in Raman lines
Applied Physics Letters 121, 063501 (2022); https://doi.org/10.1063/5.0093350

A method to stabilize the unreconstructed MgO (111) polar surface Applied Physics Letters 121, 061601 (2022); https://doi.org/10.1063/5.0096334









# Initial nucleation of metastable $\gamma$ -Ga<sub>2</sub>O<sub>3</sub> during sub-millisecond thermal anneals of amorphous Ga<sub>2</sub>O<sub>3</sub>

Cite as: Appl. Phys. Lett. **121**, 062102 (2022); doi: 10.1063/5.0087093 Submitted: 1 February 2022 · Accepted: 17 July 2022 · Published Online: 8 August 2022







Katie R. Gann, Delesta S. Chang, Delesta S. Chang, Delesta S. Chang, David A. Muller, R. Sutherland, Delesta S. Chang, D

# **AFFILIATIONS**

- Department of Materials Science and Engineering, Cornell University, Ithaca, New York 14853, USA
- <sup>2</sup>School of Applied and Engineering Physics, Cornell University, Ithaca, New York 14853, USA
- <sup>3</sup>Kavli Institute at Cornell for Nanoscale Science, Cornell University, Ithaca, New York 14853, USA

Note: This paper is part of the APL Special Collection on Wide- and Ultrawide-Bandgap Electronic Semiconductor Devices.

a) Author to whom correspondence should be addressed: motl@cornell.edu

# **ABSTRACT**

Beta-phase gallium oxide ( $\beta$ -Ga<sub>2</sub>O<sub>3</sub>) is a promising semiconductor for high frequency, high temperature, and high voltage applications. In addition to the  $\beta$ -phase, numerous other polymorphs exist and understanding the competition between phases is critical to control practical devices. The phase formation sequence of Ga<sub>2</sub>O<sub>3</sub>, starting from amorphous thin films, was determined using lateral-gradient laser spike annealing at peak temperatures of 500–1400 °C on 400  $\mu$ s to 10 ms timescales, with transformations characterized by optical microscopy, x-ray diffraction, and transmission electron microscopy (TEM). The resulting phase processing map showed the  $\gamma$ -phase, a defect-spinel structure, first nucleating under all annealing times for temperatures from 650 to 800 °C. The cross-sectional TEM at the onset of the  $\gamma$ -phase formation showed nucleation near the film center with no evidence of heterogeneous nucleation at the interfaces. For temperatures above 850 °C, the thermodynamically stable  $\beta$ -phase was observed. For anneals of 1–4 ms and temperatures below 1200 °C, small randomly oriented grains were observed. Large grains were observed for anneals below 1 ms and above 1200 °C, with anneals above 4 ms and 1200 °C resulting in textured films. The formation of the  $\gamma$ -phase prior to  $\beta$ -phase, coupled with the observed grain structure, suggests that the  $\gamma$ -phase is kinetically preferred during thermal annealing of amorphous films, with  $\beta$ -phase subsequently forming by nucleation at higher temperatures. The low surface energy of the  $\gamma$ -phase implied by these results suggests an explanation for the widely observed  $\gamma$ -phase inclusions in  $\beta$ -phase Ga<sub>2</sub>O<sub>3</sub> films grown by a variety of synthesis methods.

Published under an exclusive license by AIP Publishing. https://doi.org/10.1063/5.0087093

Gallium oxide ( $Ga_2O_3$ ) is a promising semiconductor material, with the unique advantage that the ultra-wide bandgap  $\beta$ -phase ( $E_g \sim 4.9 \, \mathrm{eV}$ ) can be grown homoepitaxially on melt-grown bulk substrates. This allows for rapid development of device structures for high temperature, high voltage, and high frequency operation. Other applications, such as UV optoelectronics, catalysis, and gas sensing, are further enabled by the material's optical transparency and thermal and chemical stabilities. While the monoclinic  $\beta$ -phase (C2/m) is the only stable line compound in the equilibrium Ga-O phase diagram (Fig. S1 of the supplementary material), numerous additional metastable polymorphs are known including  $\alpha(R\overline{3}c)$ ,  $\gamma(Fd\overline{3}m)$ ,  $\delta(Ia\overline{3})$ ,  $\epsilon(P6_3mc)$ , and  $\kappa(Pna2_1)$ . Density functional theory calculations suggest that these polymorphs have similar

formation free energies ( $\Delta F < 0.20\,\mathrm{eV}$ ), with the  $\beta$ -phase as the most stable and the  $\gamma$ -phase as the most metastable. <sup>11</sup> Due to the small energy differences, polymorphs readily form under various growth and annealing conditions, with the  $\gamma$ -phase often forming unintentionally during the growth of other phases (e.g.,  $\beta$  and  $\kappa$ ). <sup>12–15</sup> Surface  $\gamma$ -phase often appears during  $\beta$ -phase homoepitaxy <sup>12,13</sup> and at the interface for heteroepitaxy of other phases, <sup>15</sup> with the formation depending on processing temperature and impurity (doping) concentrations. <sup>12,13</sup> The widespread appearance of the thermodynamically metastable  $\gamma$ -phase suggests that it may be the kinetically favored polymorph, critically impacting the development of device-quality films.

Metastable polymorphs can readily form during annealing from high free energy states (e.g., amorphous), especially in the absence of any biasing crystallographic templates and at high thermal quench rates. Laser spike annealing (LSA), originally developed to activate dopants in silicon, 16,17 is based on scanning a focused laser across a thin film on submillisecond to millisecond time scales to achieve thermal ramp and quench rates up to 107 K/s; 18 this provides an experimental route to capture and characterize these metastable phases. A variant of LSA, lateral gradient laser spike annealing (lgLSA), intentionally varies the laser intensity laterally across the beam to enable high-throughput studies of the annealing behavior on the 100  $\mu$ s to 10 ms timescales with peak temperatures up to the melting point of the substrate. Using lgLSA, we have determined the phase formation sequence for amorphous Ga<sub>2</sub>O<sub>3</sub> on untemplated SiO<sub>2</sub> as a function of annealing time and temperature. Understanding the initial metastable polymorph formation and the subsequent formation of the stable  $\beta$ -phase provides insight into kinetic mechanisms active during growth and ultimately may lead to strategies for avoiding undesirable polymorphs in device films.

Thermally oxidized (200 nm SiO<sub>2</sub>) highly doped (p-type, 0.02  $\Omega$  cm, 100 mm) Si wafers, with lithographically patterned gold alignment marks, were prepared as substrates. The amorphous Ga<sub>2</sub>O<sub>3</sub> films were deposited by room temperature RF magnetron sputtering from an AJA Ga<sub>2</sub>O<sub>3</sub> target (99.99%. purity) at 5 mTorr pressure (9:1 Ar:O<sub>2</sub>, 10 sccm total) in a load-locked AJA system (base pressure 5  $\times$  10<sup>-8</sup> Torr). Sputtering at 210 W for 60 min with substrate rotation yielded uniform 175 nm thick films with <5% variation [cross section shown in Fig. 1(c)].

After deposition, the films were lgLSA processed using a 120 W  $CO_2$  laser ( $\lambda = 10.6 \,\mu\text{m}$ ) focused to a full width at half-maximum (FWHM) of 80  $\mu m$  in the scan direction and a nominally Gaussian profile laterally with a FWHM of  $\sim$ 510  $\mu$ m [Fig. 1(a)]. The laser power and scan velocity were controlled for individual anneal stripes (5 mm in length and spaced 2 mm laterally to minimize thermal interference), with each stripe characterized by a peak center anneal temperature ( $T_{peak}$ , center of the laser profile) and a dwell time ( $\tau$ , defined as the FWHM in the scan direction divided by the scan velocity).<sup>18</sup> Peak temperatures at the stripe center were calibrated using thermoreflectance and melt thresholds, as detailed in the supplementary material (Fig. S2). A uniform sampling of dwell times and center temperatures ( $\sim$ 25 dwells between 400  $\mu$ s and 10 ms and 25 temperatures from 500 to 1400 °C) was used with 616 unique conditions; stripes were randomly located over the 100 mm wafer to avoid systematic bias. Due to the lateral Gaussian laser intensity profile [Fig. 1(b)], each stripe included data on thermal anneals from room temperature (on stripe edges where the laser intensity is low) to the maximum temperature at the stripe center; this enabled high-throughput characterization of the impact of temperature on phase formation within each stripe (at a fixed dwell).

The dwell time serves as a surrogate experimental parameter that is directly correlated with the thermal heating and quench rates, with average values of approximately  $2T_{peak}/\tau$ . Quantitative rates, as a function of time during the laser scan, can be determined by thermoreflectance, as detailed in the supplementary material (Fig. S3).

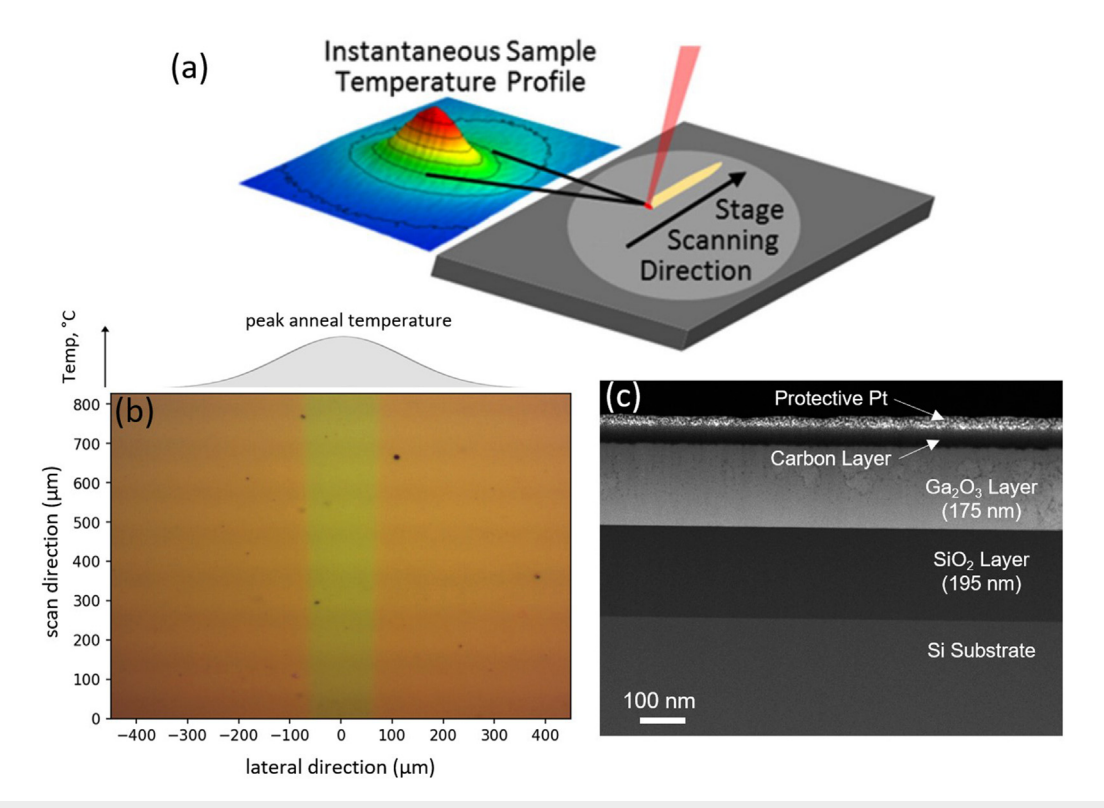


FIG. 1. (a) Schematic of a IgLSA setup with lateral temperature profile and scanning direction, showing anneal stripes; (b) example of optical micrograph after IgLSA with visible transformations and the lateral temperature gradient schematically shown above; and (c) example of a cross-sectional TEM sample showing the film stack.

The anneal stripes were characterized using optical imaging, wide-angle x-ray diffraction (XRD), and scanning transmission electron microscopy (STEM). Figure 1(b) shows an optical micrograph of an annealed lgLSA stripe, with unannealed material on the edges and the highest anneal temperature in the center. The lateral peak temperature profile [top of Fig. 1(b)] shows the expected symmetry of the heating profile across the anneal stripe, with the well-calibrated temperature at the center. A Helios G4-UX Focused ion beam (FIB) was used to prepare cross-sectional samples for STEM, using protective carbon and platinum layers to prevent ion beam damage. STEM imaging was performed with an aberration corrected Titan Themis operating at 300 keV.

XRD data were collected at the Cornell High Energy Synchrotron Source (CHESS) ID3B beamline using a 9.7 keV beam, incident at a 2° glancing angle, and focused to a  $20 \times 40 \,\mu\text{m}^2$  spot on the sample (long axis aligned along the stripe). 2D XRD images were collected using a Pilatus 300K detector (640 × 480 pixels). For each stripe, 101 images were obtained every 10 µm across the temperature gradient with a 50 ms integration time [Fig. 2(a)]. Images were calibrated using gold pads and transformed to  $q-\chi$  space [Fig. 2(a) inset], where q is the absolute value of the momentum transfer between the incident and the scattered wavevectors  $(q = |\vec{q}|)$ . Images were then integrated along the azimuthal angle,  $\chi$ , to yield conventional q–I (intensity vs q) plots [Fig. 2(b)]. 19 The final dataset consisted of 101 q-I patterns for each of the 616 stripes. Phase identification was based on *q–I* patterns, while q– $\chi$  images provided grain size and texturing information. For texture analysis, the background was approximated from the first and last 15 scans (nearly as-deposited materials).

Only three distinct phases were observed in the XRD data, with transformations well correlated with observed optical transitions. For peak anneals below 600 °C, the XRD data showed only amorphous rings with slight shifts arising from thermally induced densification. At temperatures from  $\sim$ 650 to 800 °C, and for all dwell times, the  $\gamma$ -phase ( $Fd\overline{3}m$ ) was observed; Figs. 2(d) and 2(e) show the measured XRD with the corresponding ICSD stick pattern for this defective spinel  $\gamma$ -phase. <sup>20</sup> Peak positions align well, and peak intensity ratios and broadening are reasonable given the small crystallite size, low crystallinity, and cation disorder often observed in the  $\gamma$ -phase. <sup>21–24</sup> For peak temperatures above 850 °C, the XRD data [Figs. 2(b) and 2(c)] showed the formation of highly crystalline  $\beta$ -phase (C2/m); <sup>25</sup> peak heights vary with the dwell time, suggesting film texturing at long dwells as discussed below.

To visualize the phase behavior along the lateral temperature profile, diffraction patterns were stacked as heat maps [Fig. 3(c) with x-ray intensity as color]; these maps directly correlate with corresponding optical images [Fig. 3(a)]. XRD identified phase transformations align with observed optical property changes, with two distinct regions in Fig. 3(a) and three in Fig. 3(b). For the  $760\,^{\circ}$ C and  $10\,$ ms anneal [Figs. 3(a) and 3(c)], the peak center temperature remains sufficiently low that only quench to the  $\gamma$ -phase is observed. A similar anneal to a peak center temperature of  $1360\,^{\circ}$ C exhibited quench to both  $\gamma$ - and  $\beta$ -phases [Fig. 3(d)]. (Note that optical images and XRD data were acquired at slightly different locations along the stripe, resulting in slight variations in the position of transitions on the lateral gradient.) The width of the boundaries between phases can be estimated from the optical images, where the  $1\,\mu m$ 

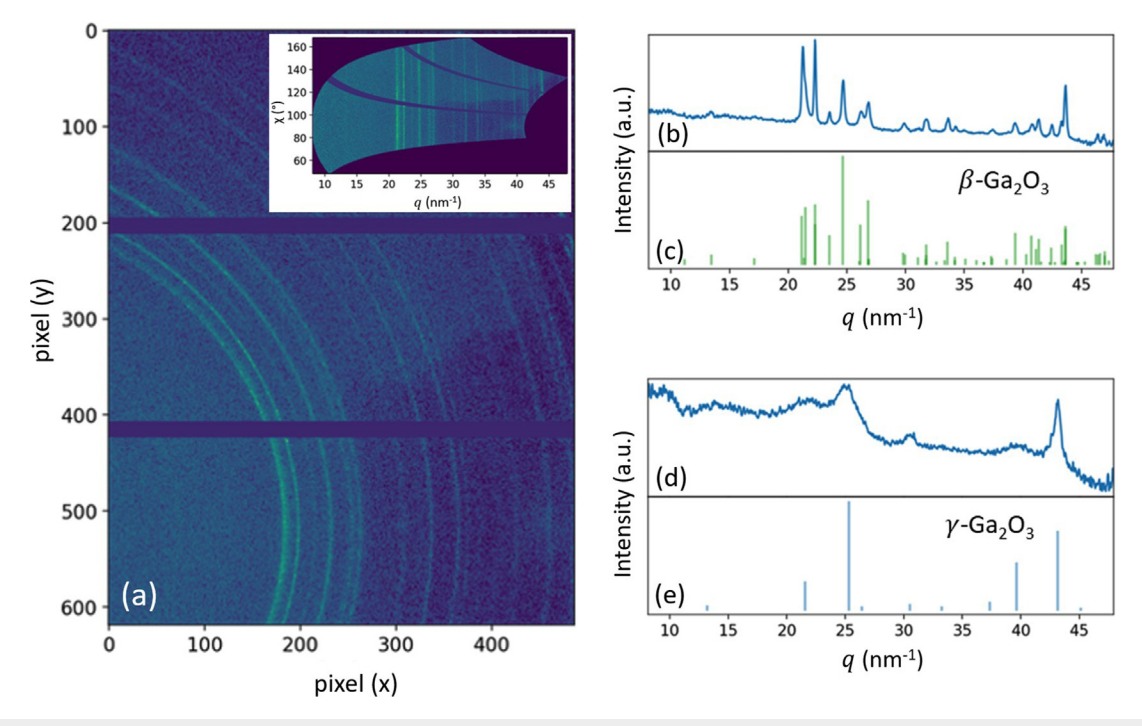
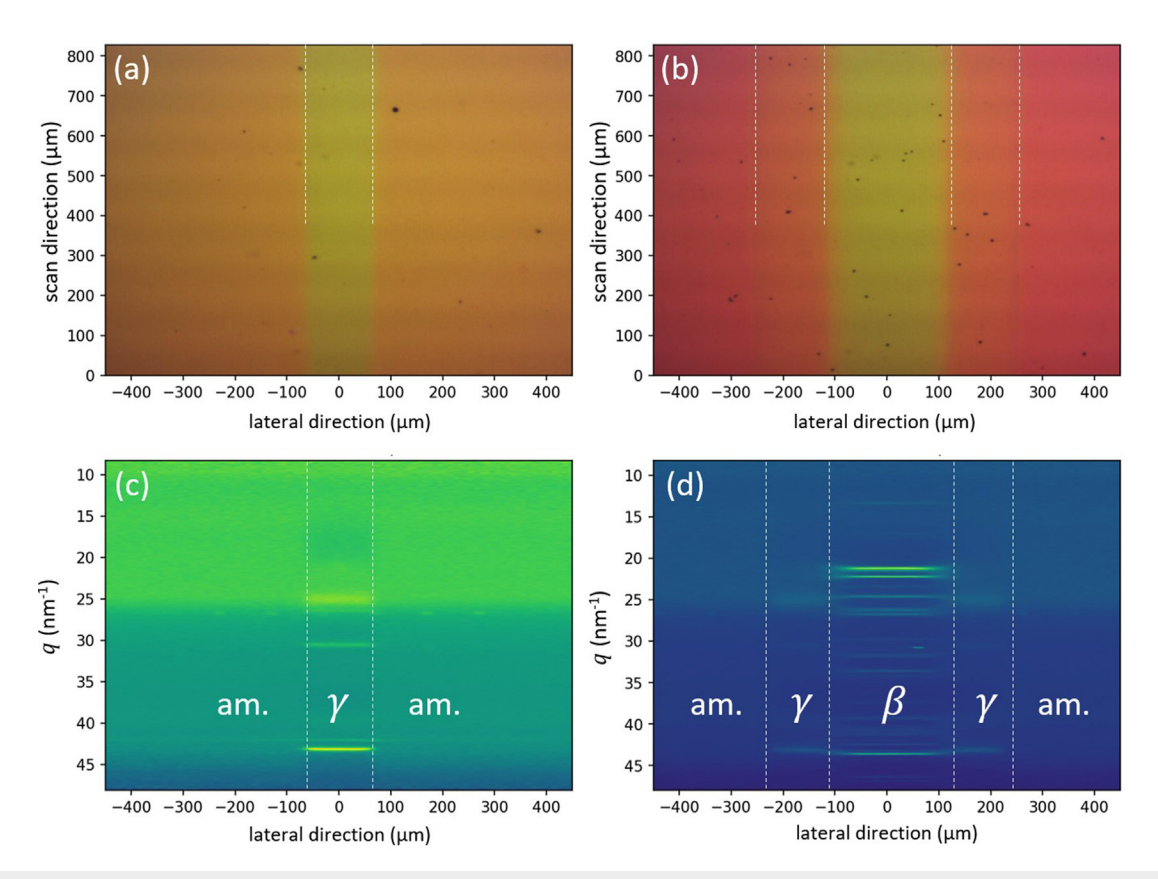


FIG. 2. (a) 2D diffraction image of  $\beta$ -Ga<sub>2</sub>O<sub>3</sub> at 1280 °C and 1.2 ms dwell time with inset transformed to the  $q-\chi$  space; (b) integrated diffraction pattern of  $\beta$ -phase formed at 1280 °C and 1.2 ms dwell time with (c) reference powder diffraction diagram; (d) integrated diffraction pattern for  $\gamma$ -phase formed at 760 °C and 10 ms dwell time with (e) reference powder diffraction diagram.



**FIG. 3.** (a) Optical image of the stripe annealed at 760 °C and 10 ms dwell time showing one optical transition; (b) optical image of the stripe annealed at 1360 °C and 10 ms dwell time showing two optical transitions; (c) stacked 1D integrated XRD patterns across the low temperature stripe, identifying amorphous and  $\gamma$ -phase; and (d) stacked 1D integrated XRD patterns of the high temperature stripe identifying amorphous,  $\gamma$ -, and  $\beta$ -phases.

resolution is significantly better than the  $10\,\mu\mathrm{m}$  XRD resolution. In Fig. 3(b), the amorphous to  $\gamma$ -phase transformation was relatively sharp (10–20  $\mu\mathrm{m}$ ), while the  $\gamma$ - to  $\beta$ -phase transformation was as broad as  $60\,\mu\mathrm{m}$ . Combined with the XRD data showing both  $\gamma$ - and  $\beta$ -phases in this zone, we suggest that there was some temperature band with two-phase coexistence.

While the relative peak height ratios of the  $\gamma$ -phase were nearly independent of the dwell time,  $\beta$ -phase XRD peak height ratios varied with dwell, indicating texturing at long dwells. This texturing is most evident in the intensity variations along diffraction rings in the raw 2D XRD [Fig. 4(a)], with strong forward scattering ( $\chi = 90^{\circ}$ ) near  $q = 21.2 \,\mathrm{nm}^{-1}$  [corresponding to (400), (110), and (40 $\overline{1}$ ) planes] and reduced scattering intensity in the forward direction at  $q = 24.6 \text{ nm}^{-1}$ corresponding to the (111) planes. To avoid the complexity of overlapping peaks, the deviation of intensity with  $\chi$  for the (111) reflection at  $q = 24.6 \text{ nm}^{-1}$  was used as a metric of the texturing, based on the quadratic coefficient of a simple quadratic fit to the XRD intensity as a function of  $\chi$  (see the supplementary material and Fig. S4 for details). Figure 4(c) shows this texturing metric for all films, exhibiting  $\beta$ -phase as a function of peak temperature and dwell. For low temperatures or short dwells, texturing was minimal but became significant for high temperatures (>1200 °C) and long dwells (>4 ms). Based on the texture development at high temperature and long times, we suggest that texturing is thermally induced.

For shorter dwells, diffraction pattern peak intensities become consistent with randomly oriented grains (Fig. S5 of the supplementary material). However, under short dwell (<1 ms) and high temperature (>1200 °C) anneals, 2D XRD patterns indicated the presence of a number of large grains, based on intense diffraction spots observed along the rings in Fig. 4(b). To quantify this behavior, the probability distribution of high intensity peaks (above background) along  $\chi$  was determined for the  $q = 22.3 \text{ nm}^{-1}$  reflection; with large grains scattering with a high intensity present as outliers in this distribution. A simple boxplot outlier detection method was used, counting the number of pixels with intensity exceeding three times the interquartile range (IQR) from Q3. The number of these outliers is shown as a function of dwell and peak center temperature in Fig. 4(d); outliers occurred most often at high temperature and short dwells, but significant numbers persisted even for the lowest anneal temperatures (800 °C). The increasing temperature required at increasing dwells suggests that the formation of large grains is linked to either the thermal heating or quench rates, both of which scale as  $2T_{peak}/\tau$ .

Figure 5, a processing phase map, summarizes the phase and morphology behavior of laser annealed films as a function of dwell and peak center anneal temperatures for each of the 616 unique stripes. For anneals below  $\sim$ 650 °C, films remained amorphous for all dwells. Between  $\sim$ 650 and  $\sim$ 800 °C, films quenched to a low crystallinity  $\gamma$ -phase, with a narrow two-phase coexistence region ( $\beta + \gamma$ )

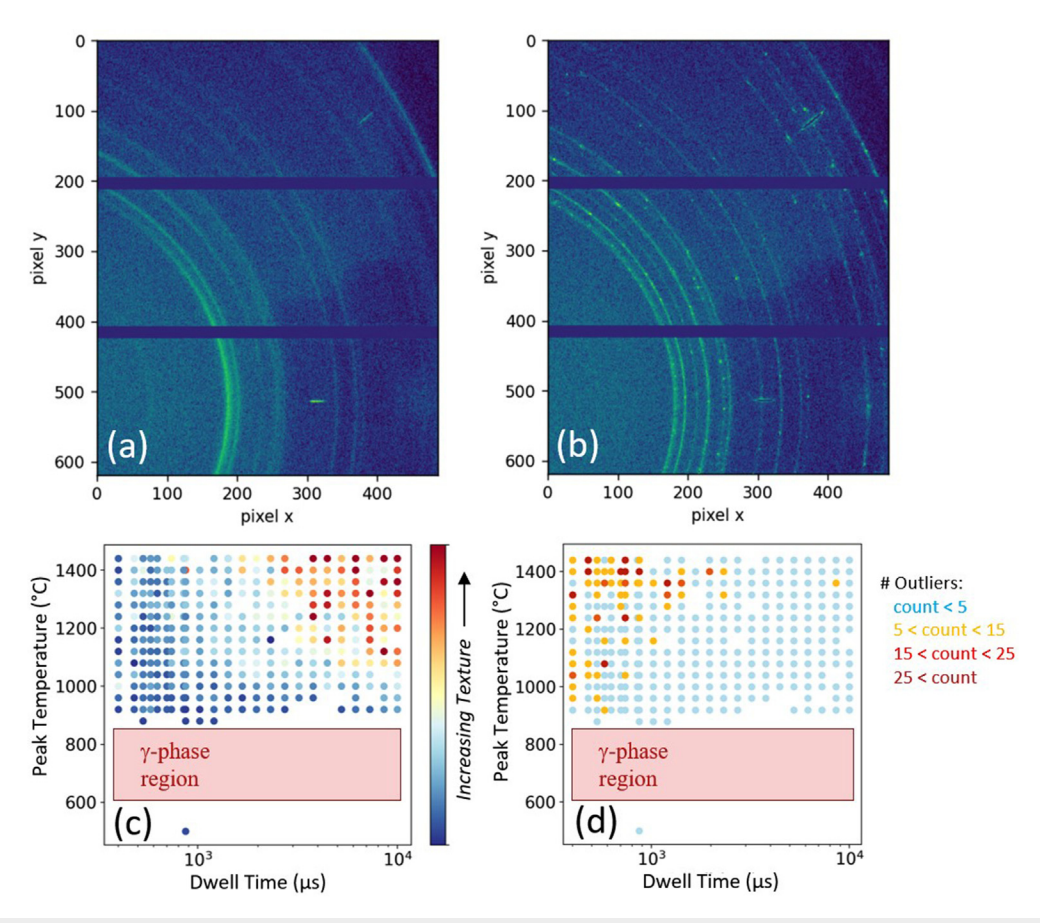


**FIG. 4.** (a) 2D diffraction pattern for high temperature, long dwell anneal condition showing texturing (uneven distribution of intensity along  $\chi$ ); (b) 2D diffraction pattern for high temperature, short dwell anneal indicating large grain formation in films ("spotty" diffraction along  $\chi$ ); (c) metric of  $\beta$ -phase texturing as a function of dwell time and peak anneal temperature; and (d) count of outliers indicating large grain density as a function of dwell time and peak anneal temperature. (Note that radial marks in the diffraction images are measurement artifacts and were masked out for analysis.)

that could not be clearly resolved within the processing temperature grid (40 °C). Within the  $\beta$ -phase region above  $\sim$ 850 °C, large grains were observed at short dwells and high temperature, and textured films were observed for long dwells and high temperature. There was a slight indication that the temperature for both phase transformations increased with dwell time, but the change was within the uncertainty of temperature calibrations and, consequently, we conclude that transformation temperatures were relatively independent of dwell. This diagram provides a road map for lgLSA time and temperature conditions to achieve the different phases and film morphologies reported. The formation of the γ-phase across all explored dwell times at temperatures lower than the  $\beta$ -phase suggests that, when thermally processing high-energy amorphous films, the  $\gamma$ -phase is a kinetically favored intermediate that forms prior to the  $\beta$ -phase. Given the weak dwell dependence, these results also suggest that it should be possible to form γ-phase even for traditional furnace annealing time frames. This was confirmed by annealing similar films of amorphous Ga2O3 at 500 °C for 2 h (Fig. S6 of supplementary material).

The cross-sectional STEM imaging was used to confirm the XRD phase identification and elucidate the onset of crystallization from the

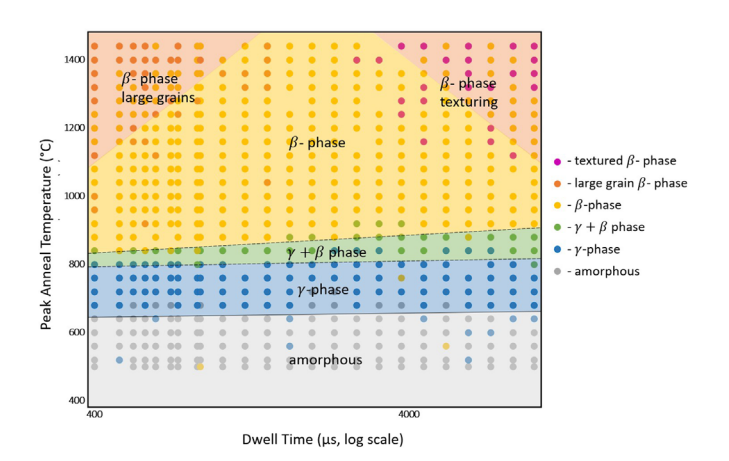


**FIG. 5.** Phase processing map for  $Ga_2O_3$  as a function of peak processing temperature and dwell time; boundaries are labeled as a guide to the eye. Specific results are shown in the legend for each dwell/temperature condition. The width of the  $\gamma + \beta$  region is approximate.

amorphous film. FIB samples were taken from a stripe annealed to a peak center temperature of  $1320\,^{\circ}\text{C}$  for  $8.6\,\text{ms}$ , corresponding to the formation of  $\beta$ -phase at the stripe center with only slight texturing. With the lgLSA technique, the anneal temperature decreases away from the maximum at the center, allowing all annealing temperatures to be examined by looking at one stripe. Figure 6(e) shows locations of the specific samples extracted, with samples taken from regions corresponding to the onset of  $\gamma$ -phase, the transition from a fully developed  $\gamma$ -phase to a fully developed  $\beta$ -phase, and near the center at the peak temperature with only  $\beta$ -phase.

Figure 6(a) shows a cross-sectional image at the first onset of  $\gamma$ -phase formation near 650 °C after annealing. (Note that dark areas in multiple TEM micrographs are likely voids that formed during heating or phase transformations.)  $\gamma$ -phase grains are observed throughout the thickness of the film, though primarily near the center, and with no nuclei observed at the SiO<sub>2</sub> interface or at the free surface. This confirms that nucleation occurred within the film, potentially homogeneously or from existing defects (potentially including voids). The high-resolution lattice image in Fig. 6(f) unambiguously confirms the  $\gamma$ -phase structure. Figures 6(b) and 6(c) are from a single 20  $\mu$ m wide FIB sample, at a higher anneal temperature close to the center of the stripe, showing the transition from nearly pure  $\gamma$ -phase on one edge [Fig. 6(b)] to nearly pure  $\beta$ -phase on the other edge [Fig. 6(c)]. The high-resolution lattice image in Fig. 6(g) again confirms the

 $\beta$ -phase structure. Finally, Fig. 6(d) is an image from a sample extracted at the center of the lgLSA stripe, at the maximum anneal temperature, showing the formation of larger  $\beta$ -phase grains at this high temperature. The absence of columnar grains further confirms the absence of heterogenous nucleation of either  $\gamma$ - or  $\beta$ -phases at the interfaces.

While the minimal dwell time dependence for transformations suggests rapid nucleation of both the  $\gamma$ - and  $\beta$ -phases above critical transformation temperatures, a key question is whether formation of the  $\beta$ -phase occurred via nucleation from remnant amorphous phase during heating or if the  $\beta$ -phase nucleated off of  $\gamma$ -phase grains that are formed during heating. Figure 6(b) shows that the film was completely transformed from amorphous to  $\gamma$ -phase before any  $\beta$ -phase was observed and that the temperature band for  $\gamma$ -phase is nearly dwell independent, we hypothesize that the  $\beta$ -phase nucleated on  $\gamma$ -phase grains after the film fully transformed. This hypothesis is consistent with the observed dwell dependence for the formation of large grains and texturing. For short dwells, rapid heating through the  $\gamma$ -phase nucleation regime will reduce the number of  $\gamma$ -grains available for  $\beta$ -phase nucleation, resulting in a shift of the grain size distribution to larger sizes, reflected in the "spotty" diffraction rings. The ramp rate is the critical parameter in this observation and higher peak temperature anneals will further reduce the time spent within the nucleation window. As the dwell time increases, the density of nucleation sites for

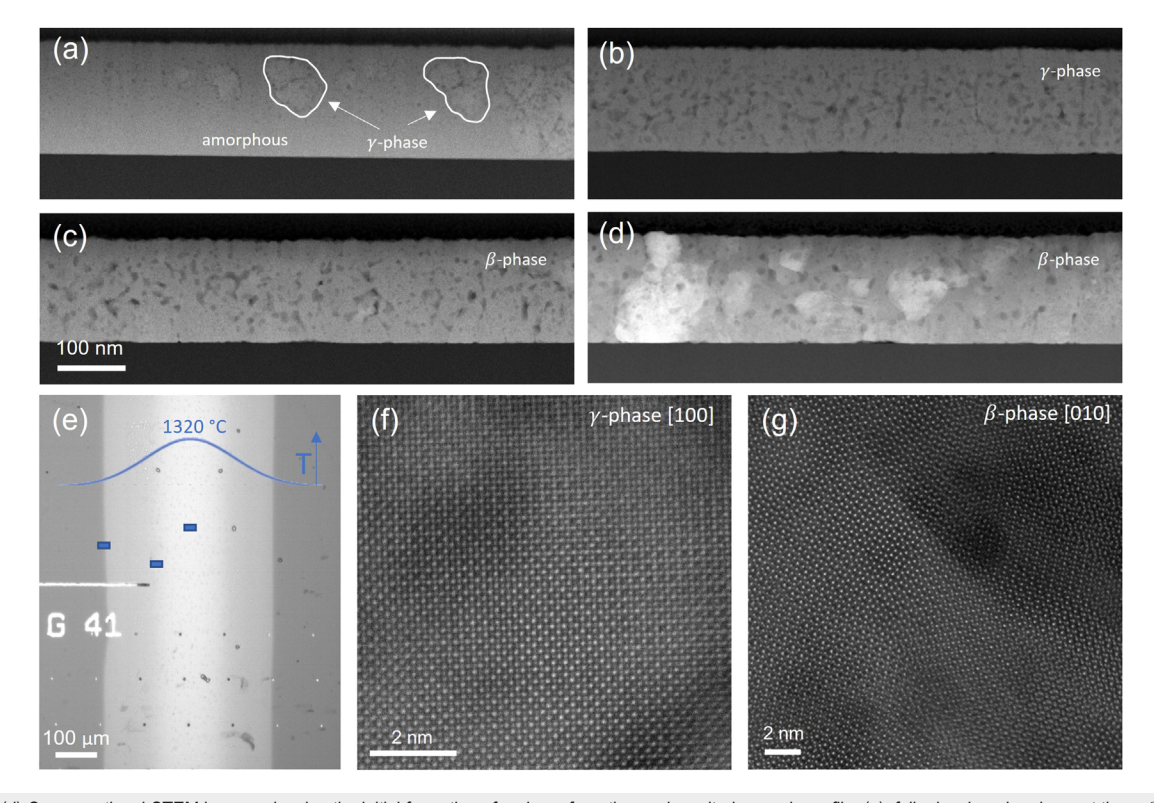


FIG. 6. (a)–(d) Cross-sectional STEM images showing the initial formation of  $\gamma$ -phase from the as-deposited amorphous film (a), fully developed  $\gamma$ -phase at the  $\gamma$ - $\beta$  phase transition (b), fully developed  $\beta$ -phase in the transition (c), and  $\beta$ -phase at the peak temperature with visible large grains on a 100 nm scale (d); (e) large area optical image of the lateral stripe with FIB sections marked in blue and schematic of Gaussian temperature profile; and (f)–(g) enlarged STEM lattice images from (a) and (d) confirming the  $\gamma$ -phase (f) and  $\beta$ -phase (g).

the  $\beta$ -phase increases, by either increasing the size or number of  $\gamma$ -phase nuclei, resulting in increased  $\beta$ -phase nucleation and eventually grain refinement at the longest dwell times and slowest ramp rates.

An equally critical question is what fundamentally determines the initial nucleating phase. Bell et al.<sup>27</sup> observed initial nucleation of a high symmetry disordered cubic structure during short dwell anneals of Bi<sub>2</sub>O<sub>3</sub>, with the formation of lower symmetry phases only for higher temperatures and longer times. We hypothesize that this is a common characteristic in this time regime, where nucleation favors high symmetry phases with small and simple unit cells and structures that can tolerate significant structural disorder. γ-Ga<sub>2</sub>O<sub>3</sub> is a defective spinel with oxygen anions in a cubic close packed (ccp) structure and gallium cations distributed on multiple octahedral and tetrahedral sites. In equilibrium, gallium occupies 54% of the (8a) Wycoff sites, 61% of the (16d) sites, 11.8% of the (48f) sites, and 10% of the (16c) sites.<sup>20</sup> Retaining the nominal  $\gamma$ -phase structure still permits a wide variation in the specific locations of cations, reducing the free energy cost for nucleation as compared to fully defined crystal structures such as the β-phase [C2/m] with 100% Ga occupancy of two inequivalent (4i) sites].

The  $\gamma$ -phase is widely observed as a defect within the equilibrium  $\beta$ -phase, arising during growth or processing of single crystal films  $^{12,13}$  and in other polymorphs.  $^{14,15}$  The low surface energy of the  $\gamma$ -phase, implied by the initial nucleation at low temperatures, presents a likely explanation for the low kinetic barrier to formation of  $\gamma$ -phase at interfaces of other phases. Given the low nucleation barrier for  $\gamma$ -phase from the disordered amorphous  $Ga_2O_3$ , it is reasonable that the energy barrier would be similarly low for other disordered interfaces, including heteroepitaxial interfaces  $^{14,15}$  and free surfaces.  $^{12,13}$  This provides a possible explanation for the observation of  $\gamma$  as a "ubiquitous defect" in  $Ga_2O_3$  films, especially for growth temperatures below the observed  $\gamma \to \beta$  transformation near 850 °C.

The metastable phase formation sequence from amorphous Ga<sub>2</sub>O<sub>3</sub> on a non-crystalline, neutral substrate was determined following laser spike annealing to peak temperatures near 1400 °C with dwells between 400 µs and 10 ms. The first phase to form with increasing temperature, for all dwells, was the γ-phase at 650 °C with nucleation occurring within the bulk of the film. The thermodynamically stable  $\beta$ -phase only formed for peak anneal temperatures above 850 °C, and no other polymorphs were observed in the quenched samples. Within the  $\beta$ -phase, large grains were observed for short dwells and high temperatures, and texturing was observed for long dwells. Based on the observation of large  $\beta$ -phase grains at the highest ramp rates and persistence of the  $\gamma$ -phase for all dwells, we hypothesize that the transformation from  $\gamma$ - to  $\beta$ -phase occurs by heterogeneous nucleation at existing  $\gamma$ -phase sites rather than from nucleation within the amorphous matrix. Initial formation of  $\gamma$ -phase also suggests that the surface energy of the γ-phase in a highly disordered matrix and the energy barrier for nucleation are remarkably low. We hypothesize that this is due to the tolerance of disorder that is characteristic of the defective-spinel  $\gamma$ -phase, and we suggest that this low barrier to nucleation helps explain the observation of  $\gamma$ -phase defect inclusions in films of  $\beta$ -Ga<sub>2</sub>O<sub>3</sub> and other polymorphs. These results will help guide future efforts to achieve defect-free β-Ga<sub>2</sub>O<sub>3</sub> for technological applications.

See the supplementary material for discussions of the Ga–O phase diagram and metastable polymorphs, detailed temperature calibration methods including heating and cooling rates, further discussion of texturing developing in longer dwell times, and furnace annealing experiments.

The authors would like to thank Vidit Gupta and Max Amsler for their help with sample preparation and x-ray measurements. This research was supported by the Air Force Research Laboratory-Cornell Center for Epitaxial Solutions (ACCESS) under Grant No. FA9550-18-1-0529 and by the SARA MURI funded by the Air Force Office of Scientific Research under Award No. FA9550-18-1-0136. The authors also acknowledge the use of the Cornell Center for Materials Research Shared Facilities supported through the NSF MRSEC program (DMR-1719875), the Materials Solutions Network at CHESS (MSN-C) supported by the Air Force Research Laboratory under Award No. FA8650-19-2-5220, and the Cornell NanoScale Facility, a member of the National Nanotechnology Coordinated Infrastructure (NNCI), which is supported by the National Science Foundation (Grant No. NNCI-2025233).

# AUTHOR DECLARATIONS

# **Conflict of Interest**

The authors have no conflicts to disclose.

### **Author Contributions**

Katie R. Gann: Conceptualization (lead); Data curation (lead); Formal analysis (equal); Investigation (lead); Methodology (lead); Validation (supporting); Visualization (equal); Writing - original draft (lead); Writing - review and editing (lead). Celesta S. Chang: Data curation (supporting); Investigation (supporting); Validation (supporting); Writing - original draft (supporting). Ming-Chiang Chang: Formal analysis (equal); Investigation (supporting); Methodology (supporting); Software (equal); Validation (supporting); Visualization (equal). **Duncan R. Sutherland:** Data curation (supporting); Formal analysis Investigation (supporting); Software (equal); (supporting); Visualization (equal). Aine B. Connolly: Data curation (supporting); Investigation (supporting). David A. Muller: Project administration (supporting); Supervision (supporting). Robert B. van Dover: Project administration (supporting); Supervision (supporting). Michael O. Thompson: Project administration (lead); Supervision (lead).

# **DATA AVAILABILITY**

Raw and processed data, along with Python scripts used in the analysis, are freely available on the Cornell eCommons repository at  $\frac{\text{https://doi.org/10.7298/e0s4-0w24}}{\text{findings of this study are available from the corresponding author upon reasonable request.}}$ 

## **REFERENCES**

<sup>1</sup>S. J. Pearton, J. Yang, P. H. Cary, F. Ren, J. Kim, M. J. Tadjer, and M. A. Mastro, Appl. Phys. Rev. 5, 11301 (2018).

<sup>&</sup>lt;sup>2</sup>H. Aida, K. Nishiguchi, H. Takeda, N. Aota, K. Sunakawa, and Y. Yaguchi, Jpn. J. Appl. Phys. 47, 8506 (2008).

- <sup>3</sup>Z. Galazka, K. Irmscher, R. Uecker, R. Bertram, M. Pietsch, A. Kwasniewski, M. Naumann, T. Schulz, R. Schewski, D. Klimm, and M. Bickermann, J. Cryst. Growth 404, 184 (2014).
- <sup>4</sup>M. Baldini, Z. Galazka, and G. Wagner, Mater. Sci. Semicond. Process. 78, 132 (2018).
- <sup>5</sup>S. Sharma, K. Zeng, S. Saha, and U. Singisetti, IEEE Electron Device Lett. 41, 836 (2020).
- <sup>6</sup>M. Orita, H. Ohta, M. Hirano, and H. Hosono, Appl. Phys. Lett. 77, 4166
- <sup>7</sup>M. Ogita, N. Saika, Y. Nakanishi, and Y. Hatanaka, Appl. Surf. Sci. 142, 188 (1999).
- <sup>8</sup>S. I. Stepanov, V. I. Nikolaev, V. E. Bougrov, and A. E. Romanov, Rev. Adv. Mater. Sci. 44, 63 (2016), https://www.ipme.ru/e-journals/RAMS/no\_14416/ 06\_14416\_stepanov.pdf.
- <sup>9</sup>M. Zinkevich and F. Aldinger, J. Am. Ceram. Soc. **87**, 683 (2004).
- <sup>10</sup>R. Roy, V. G. Hill, and E. F. Osborn, J. Am. Chem. Soc. 74, 719 (1952).
- <sup>11</sup>S. Yoshioka, H. Hayashi, A. Kuwabara, F. Oba, K. Matsunaga, and I. Tanaka, . Phys. 19, 346211 (2007).
- <sup>12</sup>P. Vogt, F. V. E. Hensling, K. Azizie, C. S. Chang, D. Turner, J. Park, J. P. McCandless, H. Paik, B. J. Bocklund, G. Hoffman, O. Bierwagen, D. Jena, H. G. Xing, S. Mou, D. A. Muller, S.-L. Shang, Z.-K. Liu, and D. G. Schlom, APL Mater. 9, 031101 (2021).
- 13 C. S. Chang, N. Tanen, V. Protasenko, T. J. Asel, S. Mou, H. G. Xing, D. Jena, and D. A. Muller, APL Mater. 9, 051119 (2021).
- <sup>14</sup>I. Cora, Z. Fogarassy, R. Fornari, M. Bosi, A. Rečnik, and B. Pécz, Acta Mater. 183, 216 (2020).
- <sup>15</sup>I. Cora, F. Mezzadri, F. Boschi, M. Bosi, M. Čaplovičová, G. Calestani, I. Dódony, B. Pécz, and R. Fornari, CrystEngComm 19, 1509 (2017).
- 16 T. Yamamoto, T. Kubo, T. Sukegawa, E. Takii, Y. Shimamune, N. Tamura, T. Sakoda, M. Nakamura, H. Ohta, T. Miyashita, H. Kurata, S. Satoh, M. Kase,

- and T. Sugii, in 2007 IEEE International Electron Devices Meeting (IEEE, 2007), pp. 143–146. <sup>17</sup>A. Shima and A. Hiraiwa, Jpn. J. Appl. Phys. **45**, 5708 (2006).
- <sup>18</sup>R. T. Bell, A. G. Jacobs, V. C. Sorg, B. Jung, M. O. Hill, B. E. Treml, and M. O. Thompson, ACS Comb. Sci. 18, 548 (2016).
- <sup>19</sup>G. Ashiotis, A. Deschildre, Z. Nawaz, J. P. Wright, D. Karkoulis, F. E. Picca, and J. Kieffer, J. Appl. Crystallogr. 48, 510 (2015).
- <sup>20</sup>H. Y. Playford, A. C. Hannon, M. G. Tucker, D. M. Dawson, S. E. Ashbrook, R. J. Kastiban, J. Sloan, and R. I. Walton, J. Phys. Chem. C 118, 16188 (2014).
- <sup>21</sup>C. O. Áreán, M. R. Delgado, V. Montouillout, and D. Massiot, Z. Anorg. Allg. Chem. 631, 2121 (2005).
- <sup>22</sup>C. O. Areán, A. L. Bellan, M. P. Mentruit, M. R. Delgado, and G. T. Palomino, Microporous Mesoporous Mater. 40, 35 (2000).
- <sup>23</sup>H. Hayashi, R. Huang, F. Oba, T. Hirayama, and I. Tanaka, J. Mater. Res. 26, 578 (2011).
- <sup>24</sup>H. Y. Playford, A. C. Hannon, E. R. Barney, and R. I. Walton, Chem. Eur. J. 19, 2803 (2013).
- <sup>25</sup>S. Geller, J. Chem. Phys. **33**, 676 (1960).
- <sup>26</sup>D. R. Sutherland, A. B. Connolly, M. Amsler, M. C. Chang, K. R. Gann, V. Gupta, S. Ament, D. Guevarra, J. M. Gregoire, C. P. Gomes, R. Bruce Van Dover, and M. O. Thompson, ACS Comb. Sci. 22, 887 (2020).
- <sup>27</sup>R. T. Bell, P. A. Beaucage, M. J. Murphy, A. B. Connolly, U. Wiesner, D. Ginley, R. B. Van Dover, and M. O. Thompson, Chem. Mater. 33, 4328
- <sup>28</sup>K. Gann, C. Chang, M.-C. Chang, D. Sutherland, A. Connolly, D. Muller, R. van Dover, and M. Thompson (2022). "Initial nucleation of metastable  $\gamma$ -Ga<sub>2</sub>O<sub>3</sub> during sub-millisecond thermal anneals of amorphous Ga<sub>2</sub>O<sub>3</sub>," Cornell University eCommons Repository. Dataset. https://doi.org/10.7298/